



Supplement of

Quantification of black carbon mixing state from traffic: implications for aerosol optical properties

M. D. Willis et al.

Correspondence to: M. D. Willis (megan.willis@mail.utoronto.ca) and A. K. Y. Lee (alexky.lee@utoronto.ca)

The copyright of individual parts of the supplement might differ from the CC-BY 3.0 licence.

1 SP-AMS measurements of rBC and non-refractory aerosol species

The SP-AMS was calibrated for refractory black carbon (rBC) quantification using size-selected (300 nm), dried Regal Black (Regal 400R Pigment, Cabot Corp.) particles to determine the mass based ionization efficiency of rBC (mIE_{rBC}) (Onasch et al., 2012; Willis et al., 2014). The relative ionization efficiency for rBC ($RIE_{rBC} = mIE_{rBC}/mIE_{NO_3}$) was 0.2 ± 0.05 (1σ uncertainty), as experimentally determined before removal of the tungsten vaporizer. Assuming that RIE_{rBC} is constant, IE_{NO_3} was calculated based on measured values of mIE_{rBC} and known RIE_{rBC} . The average mIE_{rBC} was 189 ± 20 ions/pg (for four independent calibrations throughout the study). Calculated IE_{NO_3} was then used with recommended relative ionization efficiencies (RIE) to quantify other, non-refractory, aerosol species associated with rBC (referred to as NR- PM_{rBC}) (Jimenez et al., 2003).

Uncertainty in rBC mass measurement (i.e., mIE_{rBC}), associated with the accuracy of selecting a known mass of Regal Black for calibration and counting the total number of particles, is $\pm 20\%$. Uncertainty in mIE_{NR-PM} (RIE_{NR-PM}), based on mIE_{rBC} , is $\pm 50\%$. Previous measurements of laboratory generated particles and ambient aerosol has suggested that RIE_{NR-PM} could be overestimated by up to a factor of two, resulting in an approximately 50% overestimation in NR-PM mass for hydrocarbon-like organic aerosol (HOA) species (Lee et al., 2015; Willis et al., 2014). Figure 2a and c of the main text shows histograms of the mass fraction of black carbon (mf_{BC}) for the “standard” RIE_{NR-PM} (i.e., 1,4, solid bars) and calculated by decreasing HOA mass by 50% (red dashed lines). Similar data are shown in Figure S1 for the non-roadside study. For the roadside study, these assumptions increase average mf_{BC} in BC-rich particles from 0.86 to 0.92, and from 0.02 to 0.03 in HOA-rich particles. Further uncertainties in absolute rBC mass measurement and mf_{BC} arise from the attribution of “refractory CO_x^+ ” species (i.e., CO_2^+ and CO^+ as rBC or organic species) (Corbin et al., 2014). In addition, the signal for CO^+ is conventionally estimated as equal to CO_2^+ in AMS measurements based on laboratory measurements of oxygenated organic fragmentation patterns. However, we may underestimate the $CO^+ : C_3^+$ ratio since this assumption may not be accurate for SP-AMS measurements if CO_x^+ signals arise from oxygenated moieties on the black carbon surface. Attribution of CO_x^+ signals has minimal impact on our results, as shown in Figure 2b and d of the main text, where the fraction of total BC (HOA) from BC-rich (HOA-rich) particles is shown assuming CO_x^+ species are either exclusively organic (solid bars) or rBC (dashed purple lines). CO_x^+ signals are conventionally removed from single particle data, due to air interferences in the unit mass resolution spectra, so a similar calculation was not possible in Figure 2a and c of the main text.

Collection efficiency (CE) for rBC-containing particles detected in the SP-AMS is determined by the extent of particle beam - laser beam overlap, or the fraction of particles crossing the IR-laser beam (Willis et al., 2014). CE for rBC-containing particles was determined in the roadside study using beam width probe measurements described in Willis et al. (2014). Ambient rBC-containing particles had an average beam width $\sigma = 0.46 \pm 0.03$ mm, which is close to, but wider than that of 300 nm Regal Black particles ($\sigma = 0.40 \pm 0.08$) used for calibration (Willis et al., 2014). Ideal absolute quantification of rBC would involve a time dependent CE either from more highly time resolved measurements of particle beam width, or from comparison with rBC coating thickness derived from a single particle soot photometer (SP2), neither of which were available here. Previous work has suggested that the collection efficiency for rBC and associated coating species is similar (i.e., the same CE can be applied) (Willis et al., 2014). For these reasons a constant collection efficiency of 0.6 was applied for absolute quantification of rBC and associated species. SP-AMS rBC

mass loadings (both denuded and ambient) correlated well ($R^2 > 0.90$) with absorption measurements (781 nm) from a co-located photoacoustic soot spectrometer (PASS-3, Droplet Measurement Techniques, Boulder, CO) (Healy et al., 2015), suggesting that the CE did not vary dramatically during the roadside study. Note that the CE applied will not impact calculations of mf_{rBC} .

2 Single particle observations - Non-roadside study

During the non-roadside study both the laser and tungsten vaporizers were used in the SP-AMS, such that rBC-containing and non-rBC particles were detected (Lee et al., 2015). Mass spectra and histograms of mf_{rBC} for HOA- and rBC-rich particle classes from the non-roadside study are presented in Figure S1 and size distributions are shown in Figure S3.

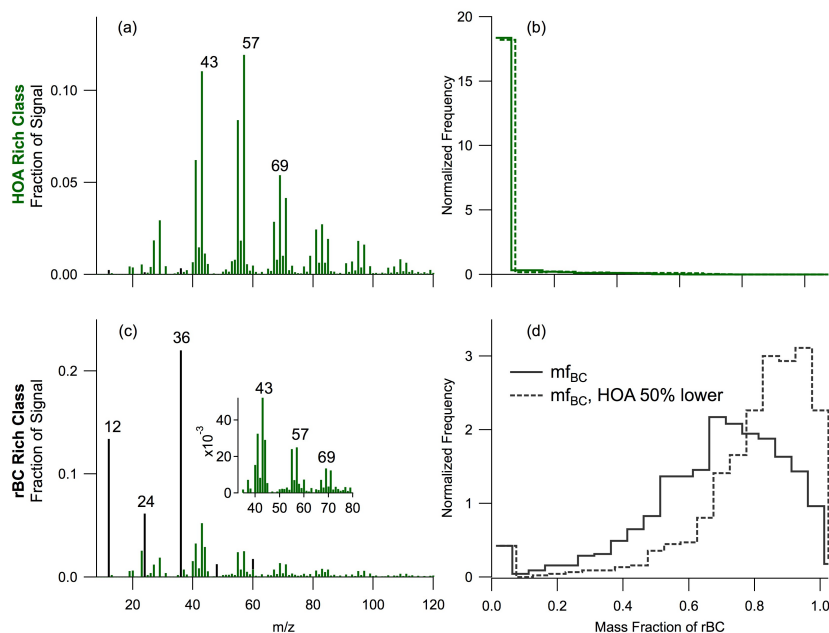


Figure S1: Single particle data from the non-roadside study: Mass spectra of HOA- (a) and rBC-rich (c) particle classes and normalized histograms of the mass fraction of rBC in the HOA- (b) and rBC-rich (d) classes. Solid lines represent mf_{rBC} calculated using an RIE_{Org} of 1.4 for HOA and dotted lines represent mf_{rBC} values calculated assuming that HOA mass was 50% lower, to represent an estimate of the uncertainty range in mf_{rBC} .

3 Estimation of coating thickness

With single particle detection capability, the LS-SP-AMS observations can be used to quantify the thickness of organic and inorganic coating on individual rBC-containing particles. This calculation focuses on determining the thickness of HOA coating derived from traffic emissions; however, oxygenated organic aerosol (OOA) and secondary inorganic species are mixed with rBC in accumulation mode particles in both urban studies (Lee et al., 2015). Transport of biomass burning organic aerosol (BBOA) was also observed during the later period of the roadside study (see Figure 4 of the main text).

A core-shell structure is assumed to determine the thickness of HOA coating on rBC-containing particles. The following assumptions are made in the calculation: a spherical rBC core, a uniform thickness of coating, and an HOA density of 0.9 g/cm^3 . To simulate the fractal structure of ambient rBC, the effective density of rBC ($\rho_{\text{eff,rBC}}$) was varied between 0.3 and 1.3 g/cm^3 , values which have been observed for laboratory soot standards and engine exhaust (Maricq and Ning, 2004; Gysel et al., 2011). Figure S2 presents the two-dimensional histograms (mf_{rBC} vs. particle aerodynamic diameter, D_{va}) of rBC- and HOA-rich particles identified by cluster analysis in the two urban studies, with calculated coating thickness curves overlaid for comparison (dashed lines). The coating thickness is relatively insensitive to variations in $\rho_{\text{eff,rBC}}$ (Figure S2, dashed line in green: 0.3 g/cm^3 , white: 0.8 g/cm^3 , and red: 1.3 g/cm^3). Note that the D_{va} of model outputs are calculated by the physical diameter (d_p) and the density (ρ_p) of particles (i.e., $D_{\text{va}} = d_p \cdot \rho_p$ where ρ_p is the linear combination of mass-weighted HOA and rBC density).

The comparisons suggest that rBC-rich particles are thinly coated by HOA-like material (Figure S2a). For example, a 200 nm (D_{va}) rBC-rich particle (i.e., physical particle diameter $\sim 245 \text{ nm}$, assuming $\rho_{\text{eff,rBC}} = 0.8 \text{ g/cm}^3$) that consists of 72-86% of rBC by mass (the average mf_{rBC} of rBC-rich particles) would be covered by 5-11 nm of HOA-like coating. In contrast, HOA-rich particles (if they contain rBC) have small rBC core sizes (Figure S2b). A 300 nm (D_{va}) HOA-rich particle (i.e., physical particle diameter $\sim 335 \text{ nm}$, assuming $\rho_{\text{eff,rBC}} = 0.8 \text{ g/cm}^3$) that co-exists with a small amount of rBC mass (3-4% by mass, the average mf_{rBC} of HOA-rich particles) has an rBC core size of 108-119 nm and a thick HOA coating (113-108 nm). These two examples illustrates that the coating thickness of HOA- and rBC-rich particles can be very different.

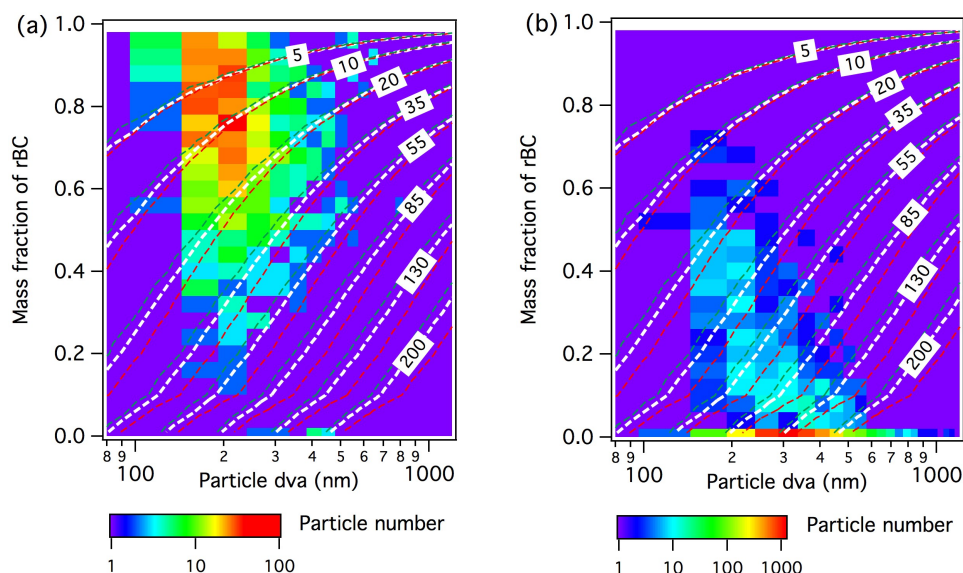


Figure S2: Two-dimensional histograms (mfrBC vs. particle aerodynamic diameter) of rBC-rich (a) and HOA-rich (b) particle classes. The color scale represents the number of particles in each particle class. The dashed lines represent the physical thickness (nm) of organic coating on rBC-containing particles determined by a core-shell structure model. To examine the potential effect of fractal structure of ambient rBC particles on predicted coating thickness, the effective density of rBC was varied (green: 0.3 g/cm³, white: 0.8 g/cm³, and red: 1.3 g/cm³) in the model calculations.

4 Ensemble and single particle size distributions

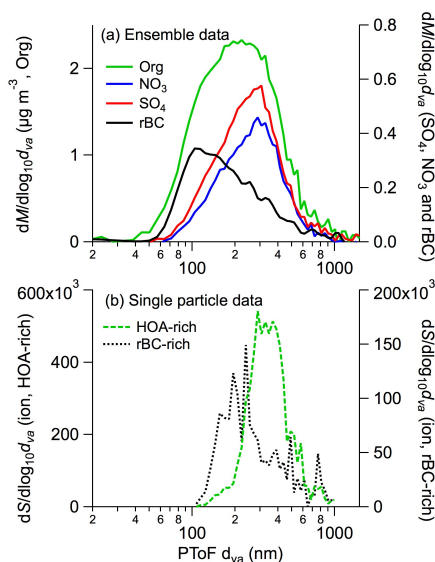


Figure S3: (a) Mass-based ensemble size distributions of rBC, organics, sulfate and nitrate in the non-roadside study. Ion signal-based single particle size distributions of (c) HOA-rich and (b) rBC-rich particle classes in the non-roadside study. Note that the LS-SP-AMS was operated in different vaporizer configurations in the non-roadside and roadside studies as discussed in the Methods section.

5 Positive matrix factorization (PMF) of ensemble measurements - Roadside study

Positive matrix factorization (PMF) was performed on the one-minute time resolution SP-AMS ensemble data to determine the sources of rBC and organic aerosol sampled in the roadside study. The bilinear model was solved using the PMF2 algorithm developed by P. Paatero (Paatero and Tapper, 1994; Paatero, 2007), in robust mode, and a four-factor solution was selected using an Igor Pro (v. 6.36, WaveMetrics, Inc.) based evaluation tool (v.2.04) according to the method described by Ulbrich et al. (2009) and Zhang et al. (2011). Time series and mass spectra of the four PMF factors are presented in Figures 4 of the main text and S4. A four-factor solution was selected as appropriate for this data set based on examination of the PMF quality of fit parameter (Q/Q_{expected}) as a function of the number of PMF factors (Figure S5). Increasing the number of factors from three to four allowed for the separation of HOA-rich and rBC-rich factors, the physical meaning of which is supported by the observation of HOA-rich and rBC-rich particle classes from single particle measurements.

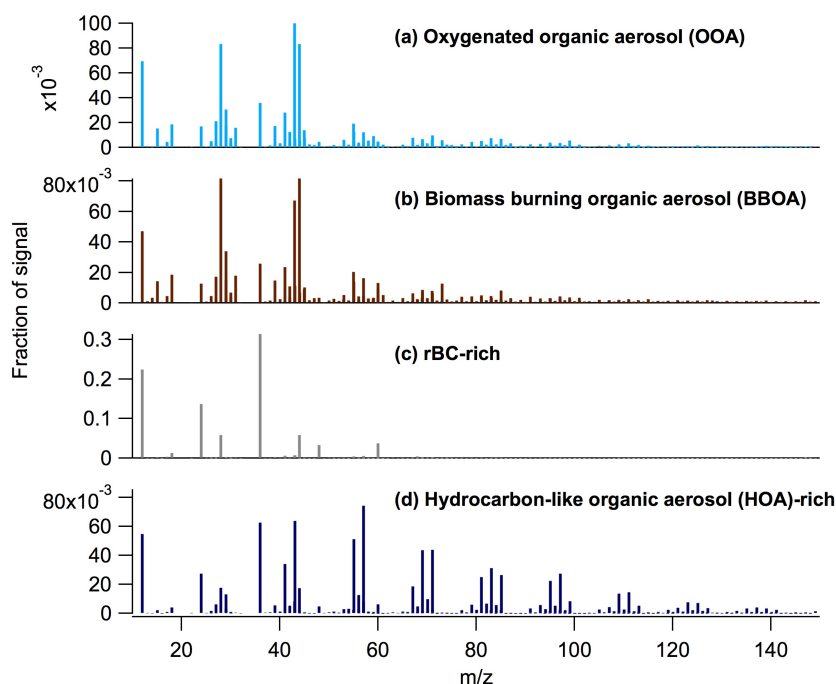


Figure S4: Ensemble data: Mass spectra of the four-factor PMF solution. The four factors represent (a) background oxygenated organic aerosol (OOA), (b) biomass burning organic aerosol (BBOA), (c) rBC-rich particles, and (d) hydrocarbon-like organic aerosol (HOA) rich particles.

6 Determination of PartMC-MOSAIC model input parameters

6.1 Step 1: Determine the mass-based ensemble size distributions of rBC and HOA from fresh traffic emissions

Figure S6 shows the size distributions of rBC and organic excluding periods with a strong influence from biomass burning. The size distributions were fitted with three log-normal

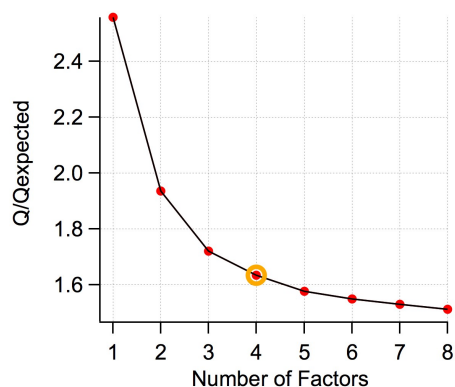


Figure S5: The PMF quality of fit parameter (Q/Q_{expected}) as a function of the number of factors.

distributions with maximum D_{va} at 96.0 (peak 1), 173.4 (peak 2) and 390.8 nm (peak 3) for both rBC and organics using the multi-peak fitting package in IGOR Pro version 6.36 (WaveMetrics, Inc.). Assuming peak 3 for both rBC and organics represents aged particles in the accumulation mode, Peaks 1 and 2 are used to represent the size distributions of the rBC and HOA originating from fresh traffic emissions.

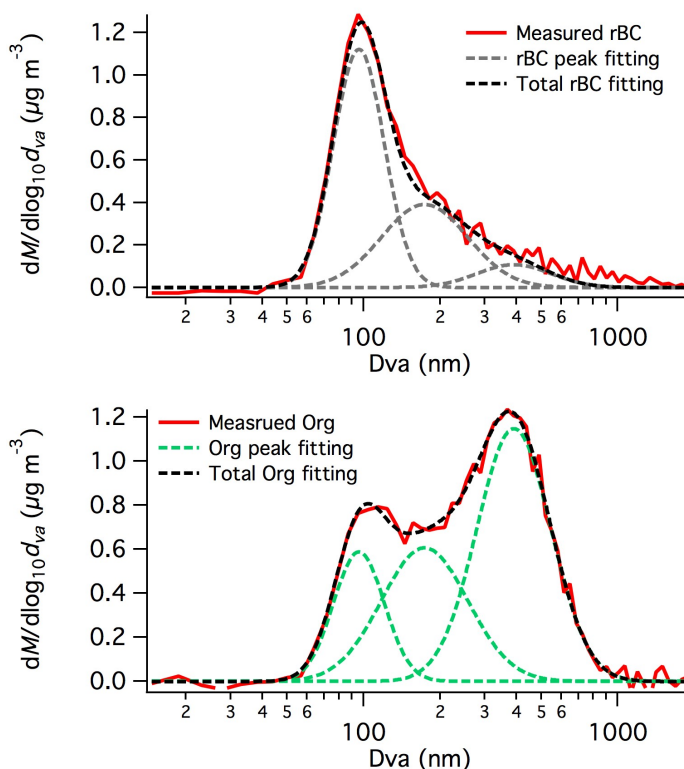


Figure S6: Size distributions of rBC (top) and organic (bottom) excluding the strong biomass burning event (red lines). The dashed lines represent the peak fitting results.

6.2 Step 2: Determine the mass-based ensemble size distributions of rBC in rBC-rich and HOA-rich particle types

According to Figure 2d in the main text, rBC-rich and HOA-rich particle types accounted for approximately 93% and 7% of the total rBC mass, respectively. The contribution of rBC-rich and HOA-rich particle types to the total rBC mass in peak 1 and 2 can be calculated using Eq. 1 and 2, respectively. The calculation results are shown in Figure S7.

$$\text{rBC}_{(\text{Peak}i, \text{rBC-rich})} = \text{rBC}_{(\text{Peak}i, \text{total})} \cdot 0.93 \quad (1)$$

$$\text{rBC}_{(\text{Peak}i, \text{HOA-rich})} = \text{rBC}_{(\text{Peak}i, \text{total})} \cdot 0.07 \quad (2)$$

where i is the peak number from step 1 (i.e. D_{va} at 96.0 nm = peak 1 and 173.4 nm = peak 2).

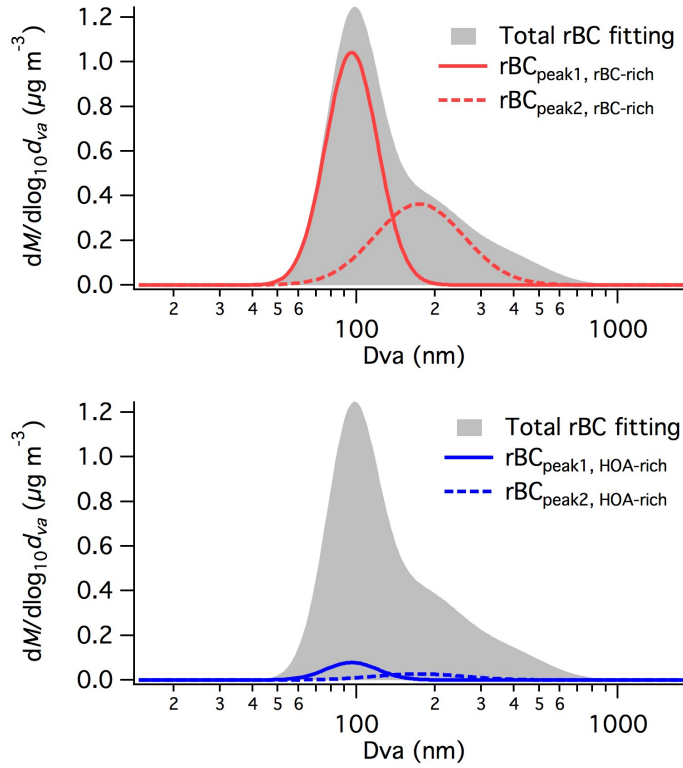


Figure S7: Size distributions of rBC in rBC-rich (top) and HOA-rich (bottom) particle types. The accumulation mode particles (i.e. peak 3 identified in step 1) are excluded in the calculation.

6.3 Step 3: Determine the mass-based ensemble size distributions of HOA in rBC-rich and HOA-rich particle types

According to Figure 2c in the main text, rBC accounted for about 86% of total mass in the rBC-rich particles. The mass of HOA materials in rBC-rich and HOA-rich particle types in peak 1 and 2 can be calculated using Eq. 3 and 4, respectively. The calculation results are shown in Figure S8.

$$\text{HOA}_{(\text{Peak}i, \text{rBC-rich})} = \frac{\text{rBC}_{(\text{Peak}i, \text{rBC-rich})}}{0.86} \cdot 0.14 \quad (3)$$

$$\text{HOA}_{(\text{Peak}i, \text{HOA-rich})} = \text{HOA}_{(\text{Peak}i, \text{total})} - \text{HOA}_{(\text{Peak}i, \text{rBC-rich})} \quad (4)$$

where i is the peak number from step 1 (i.e. D_{va} at 96.0 nm = peak 1 and 173.4 nm = peak 2)

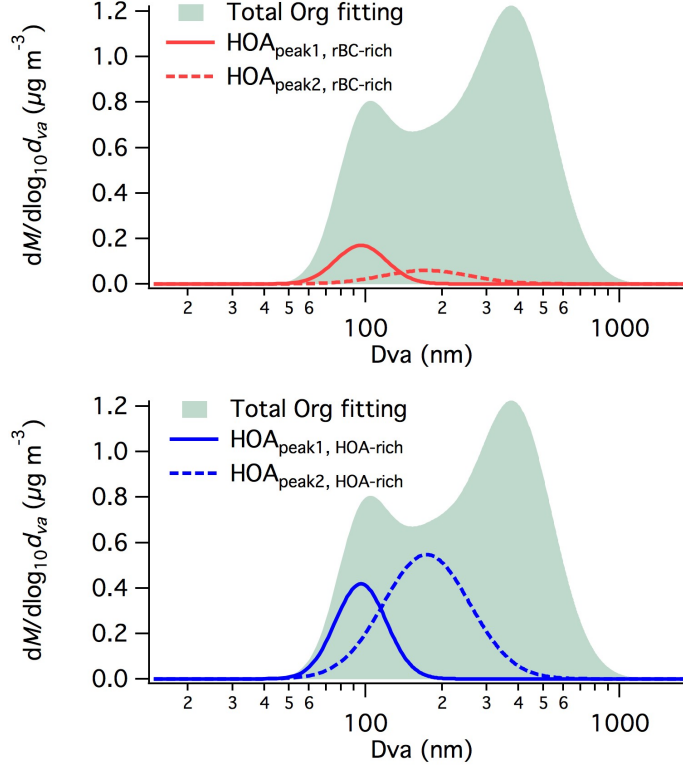


Figure S8: Size distributions of HOA in rBC-rich (top) and HOA-rich (bottom) particle types. The accumulation mode particles (i.e. peak 3 identified in step 1) are excluded in the calculation.

6.4 Step 4: Determine the mass-based ensemble size distributions of rBC-rich and HOA-rich particle types

The total size distributions of rBC-rich and HOA-rich particle classes can be calculated using Eq. 5 and 6 (i.e. summation of the rBC and HOA mass in each particle type). The calculation results are shown in Figure S9.

$$\text{Total}_{(\text{Peak}i, \text{rBC-rich})} = \text{rBC}_{(\text{Peak}i, \text{rBC-rich})} + \text{HOA}_{(\text{Peak}i, \text{rBC-rich})} \quad (5)$$

$$\text{Total}_{(\text{Peak}i, \text{HOA-rich})} = \text{rBC}_{(\text{Peak}i, \text{HOA-rich})} + \text{HOA}_{(\text{Peak}i, \text{HOA-rich})} \quad (6)$$

where i is the peak number from step 1 (i.e. D_{va} at 96.0 nm = peak 1 and 173.4 nm = peak 2)

6.5 Step 5: Calculate the number-based size distribution parameters as model inputs

The mass-based geometric diameter and geometric standard deviation of each peak for both rBC-rich and HOA-rich particle types are calculated based on the lognormal fitting param-

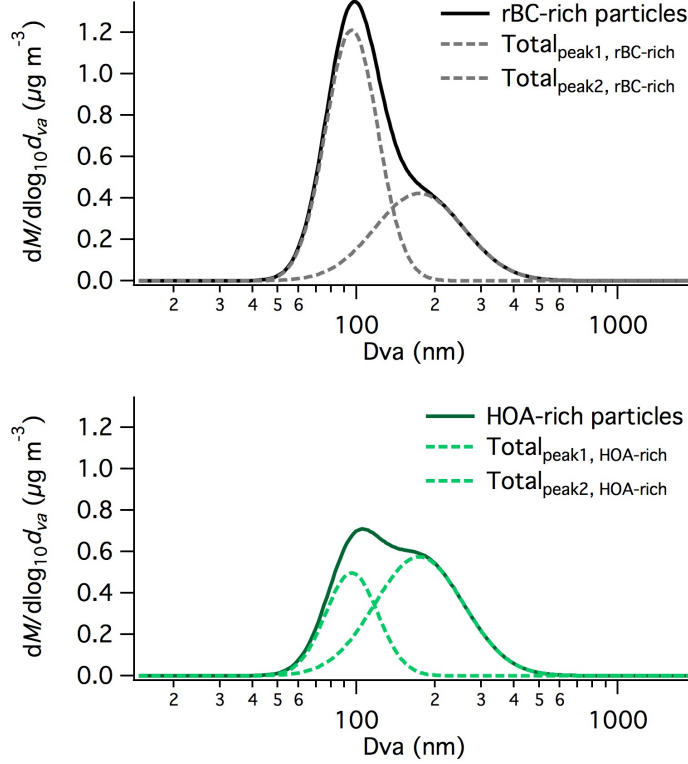


Figure S9: Size distributions of rBC-rich (top) and HOA-rich (bottom) particle types. The accumulation mode particles (i.e. peak 3 identified in step 1) are excluded in the calculation.

eters obtained from Steps 2 to 4 using IGOR Pro. After that, the mass-based geometric diameter can be transformed to the number-based geometric diameter using Eq. 7 (Seinfeld and Pandis, 2006). Note that the geometric standard deviations of mass- and number-based distributions are the same. The calculation results are shown in Table S1.

$$\ln d_{\text{pgM}} = \ln d_{\text{pgN}} + 3 \ln 2 \sigma_g \quad (7)$$

where d_{pgM} = particle mass – based geometric diameter
 d_{pgN} = particle number – based geometric diameter
 σ_g = geometric standard deviation

The mass-based (or volume-based) peak area obtained from lognormal fittings can be transformed to the number-based parameters using the following approach. The calculation results are shown in Table S1. The derived parameters can be used to constrain the ratio of rBC-rich and HOA-rich particle emission rates in the model stimulation.

The total volume (V) of a size distribution is:

$$V = \int_0^\infty n_v(d_p) d(d_p) = \int_0^\infty \frac{\pi}{6} d_p^3 n(d_p) d(d_p) \quad (8)$$

where d_p is the particle diameter. Generally, the k-th moment (M_k) of a distribution is:

$$M_k = \int_0^\infty d_p^k n(d_p) d(d_p) \quad (9)$$

The total volume is proportional to the third moment of the distribution. Combining Eq.8 and Eq. 9 and assuming spherical particles:

Table S1: Aerosol initial conditions and emissions for the measurement-constrained case. The symbol N denotes the total number concentration of the initial aerosol population in each log-normal mode, E is the flux of emitted particles, which is constant with time for the first 12 h of simulations and then stops, mf_{BC} and mf_{HOA} are the average values of BC and primary organic carbon mass fraction of the particles, and σ_{BC} and σ_{HOA} are the standard deviations around that mean

Quantity	rBC-rich particles (Peak 1, BC1)	rBC-rich particles (Peak 2, BC2)	HOA-rich particles (Peak 1, HOA1)	HOA-rich particles (Peak 2, HOA2)
mf_{BC}	0.86	0.86	0.03	0.03
mf_{HOA}	0.14	0.14	0.97	0.97
σ_{BC}	0.14	0.14	0	0
σ_{HOA}	0.14	0.14	0	0
d_{pgM} (nm)	101.0	202.4	101.0	202.4
σ_{g}^*	1.25	1.48	1.25	1.48
d_{pgN} (nm)*	86.7	128.6	86.7	128.6
Particle mass-based peak area from log-normal fitting	68.78	77.64	28.22	105.76
Particle number-based parameters (N) from Eq.11	1.97×10^{11}	4.35×10^{10}	7.45×10^{10}	5.38×10^{10}
N (m^{-3})*	1.97×10^9	4.35×10^8	7.45×10^8	5.38×10^8
E ($\text{m}^{-2} \text{s}^{-1}$)*	2×10^7	4.42×10^6	7.56×10^6	5.46×10^6

*Data used as model input

$$V = \frac{\pi}{6} M_3 \quad (10)$$

For a log-normal distribution, the integral for the k-th moment can be evaluated analytically:

$$M_k = \int_{-\infty}^{\infty} d_p^k n \cdot (\ln d_p) d(\ln d_p) = N d_{pg}^k \cdot e^{\frac{k^2}{2} \ln^2 \sigma_g} \quad (11)$$

The third moment of a mode is proportional to particle volume (or mass), and the particle number-based parameters (N) can be determined using Eq. 11 if d_{pg} and σ_g (geometric diameter and standard deviation of the particle number distribution) are available.

7 Particle-resolved aerosol box model simulations

Here we compare two simulations that differ in the way the mixing state of the aerosol initial conditions and the aerosol emissions are prescribed. The setup of the particle-resolved simulations is similar to the urban plume scenarios in Riemer et al. (2009) and Zaveri et al. (2010). Common to both simulations are the following specifics: The number of computational particles used in the simulation is about 10^5 . The total simulation time is 24 h, with a simulation start of 06:00 local standard time (LST). The initial gas phase concentrations and the dilution with the background gas and aerosol are the same as in Zaveri et al. (2010). In contrast to Zaveri et al. (2010), we prescribe a constant mixing height (400 m), relative humidity (70%) and temperature (298.15 K) to simplify the interpretation of the results. We also reduced the gas phase emissions by a factor of two compared to Zaveri et al. (2010) to create more moderately polluted conditions. The initial aerosol population was sampled from log-normal size distributions fitted from the measurement data, as shown in Table S1. To fully exploit the information supplied by the observations, we introduced a new method of sampling the aerosol composition.

The new composition-sampling method proceeds as follows. For each aerosol particle, the diameter is first sampled, and then the composition is sampled as a vector of mass fractions $\mathbf{w} = [w_{\text{BC}}, w_{\text{HOA}}]^\top$. Although we only sample two species for the simulations in this paper, we specify the sampling algorithm for any number of species. We use bold symbols to denote vectors, so \mathbf{bf} is the mean mass fraction vector from Table S1. We write Σ for the diagonal covariance matrix with diagonal entries $(\sigma_i)^2$, $\mathbf{1}$ for the vector of ones, and \mathbf{x}^\top for the transpose of a vector \mathbf{x} . We sample the composition vector \mathbf{w} from a multivariate normal distribution on the affine hyperplane of vectors that sum to one, truncated to the positive closed orthant (and thus to the probability or standard simplex). This is done as shown in Algorithm 1 using an accept-reject procedure.

Algorithm 1 Composition sampling

- 1: **repeat**
 - 2: $\mathbf{x} \leftarrow \mathcal{N}(\mathbf{mf}, \Sigma)$
 - 3: $\mathbf{w} \leftarrow \mathbf{x} + (1 - \mathbf{1}^\top \mathbf{x}) \mathbf{mf}$
 - 4: **until** $w_i \geq 0$ for all i
-

Algorithm 1 has five important properties, as follows. (1) It is clear that if the algorithm terminates then \mathbf{w} lies in the positive closed orthant, so every species has a non-negative mass fraction. (2) The sum of the sampled mass fractions \mathbf{w} is one, as can be seen from $\mathbf{1}^\top \mathbf{w} = \mathbf{1}^\top \mathbf{x} + (1 - \mathbf{1}^\top \mathbf{x}) \mathbf{1}^\top \mathbf{mf} = \mathbf{1}^\top \mathbf{x} + 1 - \mathbf{1}^\top \mathbf{x} = 1$, assuming that the mean mass fractions

sum to one and so $\mathbf{1}^\top \mathbf{mf} = 1$. (3) The distribution of \mathbf{w} is a truncated multivariate normal, which follows from the fact that \mathbf{x} has a multivariate normal distribution, \mathbf{w} is an affine function of \mathbf{x} , and the accept-reject procedure samples from the truncation of the per-iteration distribution. Note, however, that the resulting marginal distributions for each single-species mass fraction will not in general have mean and standard deviation given by mf_i and σ_i , respectively. (4) Adding additional species with zero mean mass fraction and zero standard deviation will not change the distribution of the other sampled mass fractions, as the additional species will have zero components in both \mathbf{x} and \mathbf{w} and will not alter the calculation of any other components. (5) Finally, the algorithm will terminate with probability one, under the conditions that the mean mass fractions sum to one and each σ_i is non-negative and zero only if the corresponding mf_i is non-negative. This last property can be seen by first considering the set A of \mathbf{x} that will result in a \mathbf{w} in the positive closed orthant, terminating the algorithm. This set A is exactly the direct sum of the probability simplex with the span of $\{\mathbf{mf}\}$, as can be seen by checking that $\mathbf{x} = \mathbf{p} + \alpha \mathbf{mf}$ for \mathbf{p} in the probability simplex and any scalar α results in $\mathbf{w} = \mathbf{p}$, so that the entire probability simplex is thus obtained from A . The conditions on \mathbf{mf} and the σ_i imply that \mathbf{x} has non-zero probability of lying in A , and hence the algorithm has non-zero probability of terminating on each iteration. Because each iteration is an iid Bernoulli trial, the algorithm thus terminates with probability one.

The two simulations differ in the assigned mixing state of the initial aerosol populations and the aerosol emissions. For the measurement-constrained case we distinguish between BC-rich and HOA-rich particle classes, as the observations indicate. Both classes consist of two modes, which amounts to four modes in total, as listed in Table S1. Note that the modes BC1 and HOA1 have the same geometric mean diameter and geometric standard deviation, but differ in their abundance and their emission rate, respectively. The same applies to modes BC2 and HOA2. This specific choice is guided by the observations as shown in Table S1.

For the uniform case only two modes are prescribed, with the same geometric mean diameter and standard deviation as modes BC1/HOA1 and BC2/HOA2, respectively (Table S2). The mass fractions of BC and HOA in these two modes are identical, and they are equal to the mass fractions of the bulk concentrations for the measurement-constrained case. Hence the uniform case represents conditions for which the bulk mass concentrations and the size distribution are the same as for the measurement-constrained case, but for which the detailed mixing state information is not available. A comparison of the two cases therefore quantifies the importance of mixing state information at emission for properties of interest, such as optical properties and CCN activation properties.

Figure S10 shows the temporal evolution of the bulk aerosol species over the course of the 24-h simulation. The primary species black carbon and organic carbon increase initially owing to emissions, and then decrease after emissions are discontinued at $t = 12$ h as a result of dilution with the background. The model simulations also show the production of inorganic and organic secondary aerosol species, which condense on the primary particles, continuously modifying the composition of each particle in the aerosol population. Not shown on this figure is the aerosol water content. While the particles start out dry, they take up water around $t = 6$ h when nitrate formation begins.

We calculate the optical properties at a wavelength of 550 nm and the critical supersaturations of each particle in a post-processing step according to Zaveri et al. (2010). For the optical properties we assume spherical particles with a “core-and-shell” configuration in which BC forms the particle core and the other substances compose the shell. We then use Mie calculations (Ackerman and Toon, 1981) to determine the extinction and scattering

Table S2: Aerosol initial conditions for the uniform initial mixing state case.

Quantity	Mode1	Mode2
d_{pgN} (m)	8.67	1.29
σ_g	1.25	1.48
N (m^{-3})	2.72×10^9	9.73×10^8
E ($\text{m}^{-2} \text{s}^{-1}$)	2.76×10^7	9.88×10^6
mf_{BC}	0.44	0.44
mf_{HOA}	0.56	0.56
σ_{BC}	0	0
σ_{HOA}	0	0

cross sections for each particle in the population. From these values, the volume extinction, scattering, and absorption coefficients can be reconstructed as shown in Figure 4 of the main manuscript. Note that we assume all primary and secondary organic substances to be non-absorbing, hence we do not consider any effects due to brown carbon.

To determine the critical supersaturations, we employ κ -Köhler theory (see Zaveri et al. (2010) for details). Based on the critical supersaturation values of each particle in the population, we construct CCN spectra, as shown in Figure S11 for different times throughout the simulation. As the simulation progresses, the CCN/CN fraction at low values of critical supersaturation increases, since the the particles become more hygroscopic due to the condensation of secondary aerosol material. Since both primary organic carbon ($\kappa = 0.001$) and black carbon ($\kappa = 0$) are model species with similar and low hygroscopicity parameters, the differences between the uniform case and the measurement-constrained case are small, and the two CCN spectra are almost indistinguishable.

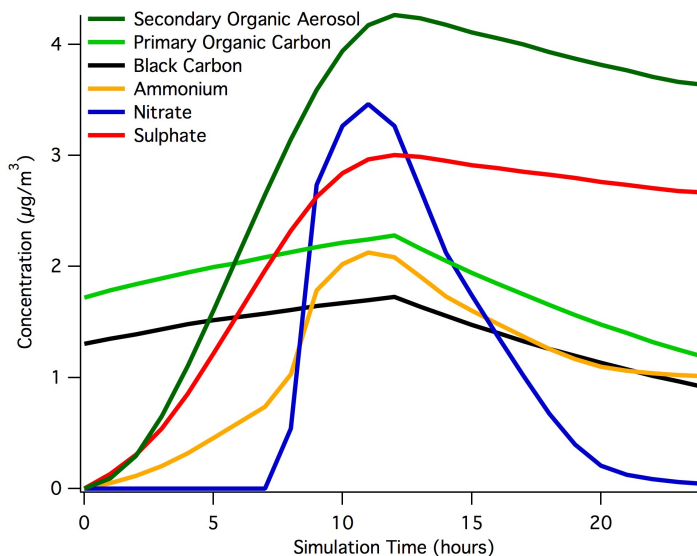


Figure S10: Mass concentrations of bulk aerosol species over the 24h simulation period in both the uniform initial and measurement constrained mixing state cases.

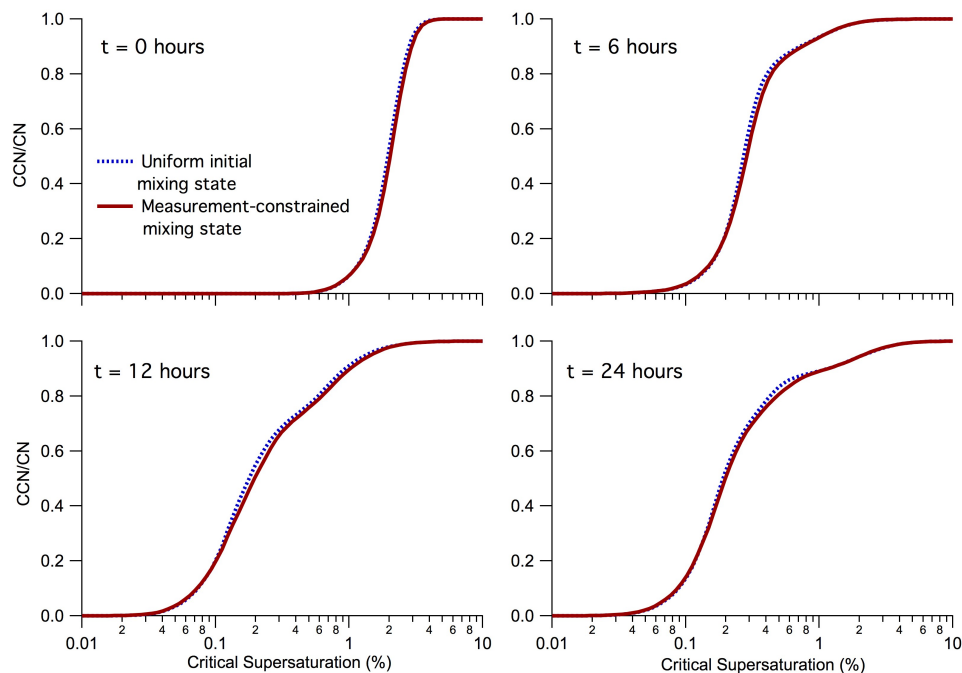


Figure S11: Modelled CCN spectra over the 24 hour simulation period for the uniform initial mixing state (dashed lines) and measurement constrained (solid lines) cases.

References

- Ackerman, T. and Toon, O.: Absorption of visible radiation in atmospheres containing mixtures of absorbing and nonabsorbing particles, *Applied Optics*, 20, 3661–3668, doi:10.1364/AO.20.003661, 1981.
- Corbin, J. C., Sierau, B., Gysel, M., Laborde, M., Keller, A., Kim, J., Petzold, A., Onasch, T. B., Lohmann, U., and Mensah, A.: Mass spectrometry of refractory black carbon particles from six sources: carbon-cluster and oxygenated ions, *Atmospheric Chemistry and Physics*, 14, 2591–2603, 2014.
- Gysel, M., Laborde, M., Olfert, J. S., Subramanian, R., and Groehn, A. J.: Effective density of Aquadag and fullerene soot black carbon reference materials used for SP2 calibration, *Atmospheric Measurement Techniques*, 4, 2851–2858, 2011.
- Healy, R. M., Wang, J. M., Jeong, C.-H., Lee, A. K. Y., Willis, M. D., Jaroudi, E., Zimmerman, N., Hilker, N., Murphy, M., Eckhardt, S., Stohl, A., Abbatt, J. P. D., Wenger, J. C., and Evans, G. J.: Light-absorbing properties of ambient black carbon and brown carbon from fossil fuel and biomass burning sources, *Journal of Geophysical Research: Atmospheres*, 120, doi:10.1002/2015JD023382, 2015.
- Jimenez, J. L., Jayne, J. T., Shi, Q., Kolb, C. E., Worsnop, D. R., Yourshaw, I., Seinfeld, J. H., Flagan, R., Zhang, X., Smith, K., Morris, J., and Davidovits, P.: Ambient aerosol sampling using the Aerodyne Aerosol Mass Spectrometer, *Journal of Geophysical Research-Atmospheres*, 108, doi:10.1029/2001JD001213, 2003.
- Lee, A. K. Y., Willis, M. D., Healy, R. M., Onasch, T. B., and Abbatt, J. P. D.: Mixing state of carbonaceous aerosol in an urban environment: Single particle characterization

- using a soot particle aerosol mass spectrometer (SP-AMS), *Atmospheric Chemistry and Physics*, 15, 1823–1841, 2015.
- Maricq, M. M. and Ning, X.: The effective density and fractal dimension of soot particles from premixed flames and motor vehicle exhaust, *Journal of Aerosol Science*, 35, 1251–1274, 2004.
- Onasch, T. B., Trimborn, A., Fortner, E. C., Jayne, J. T., Kok, G. L., Williams, L. R., Davidovits, P., and Worsnop, D. R.: Soot Particle Aerosol Mass Spectrometer: Development, Validation, and Initial Application, *Aerosol Science and Technology*, 46, 804–817, 2012.
- Paatero, P.: User’s guide for positive matrix factorization programs PMF2.exe and PMF3.exe, Tech. rep., University of Helsinki, Finland, 2007.
- Paatero, P. and Tapper, U.: Positive matrix factorization: A non-negative factor model with optimal utilization of error estimate of data values, *Environmetrics*, 5, 111–126, 1994.
- Riemer, N., West, M., Zaveri, R. A., and Easter, R. C.: Simulating the evolution of soot mixing state with a particle-resolved aerosol model, *Journal of Geophysical Research-Atmospheres*, 114, doi:10.1029/2008JD011073, 2009.
- Seinfeld, J. H. and Pandis, S.: *Atmospheric Chemistry and Physics*, 2 Ed., Jon Wiley and Sons, New York, 2006.
- Ulbrich, I. M., Canagaratna, M. R., Zhang, Q., Worsnop, D. R., and Jimenez, J. L.: Interpretation of organic components from Positive Matrix Factorization of aerosol mass spectrometric data, *Atmospheric Chemistry and Physics*, 9, 2891–2918, 2009.
- Willis, M. D., Lee, A. K. Y., Onasch, T. B., Fortner, E. C., Williams, L. R., Lambe, A. T., Worsnop, D. R., and Abbatt, J.: Collection efficiency of the soot-particle aerosol mass spectrometer (SP-AMS) for internally mixed particulate black carbon, *Atmospheric Measurement Techniques*, 7, 4507–4516, 2014.
- Zaveri, R., Barnard, J., Easter, R., Riemer, N., and West, M.: Particle-resolved simulation of aerosol size, composition, mixing state, and the associated optical and cloud condensation nuclei activation properties in an evolving urban plume, *Journal of Geophysical Research*, 115, doi:10.1029/2009JD013616, 2010.
- Zhang, Q., Jimenez, J. L., Canagaratna, M. R., Ulbrich, I. M., Ng, N., Worsnop, D., and Sun, Y.: Understanding atmospheric organic aerosols via factor analysis of aerosol mass spectrometry: A review, *Anal. Bioanal. Chem.*, 401, 3045–3067, doi:10.1007/s00216-011-5355-y, 2011.